Extraction of coherent structures in a rotating turbulent flow experiment

Jori E. Ruppert-Felsot, Olivier Praud, Eran Sharon,* and Harry L. Swinney†
Center for Nonlinear Dynamics and Department of Physics, The University of Texas at Austin, Austin, Texas 78712, USA
(Received 20 October 2004; published 25 July 2005)

The discrete wavelet transform (DWT) and discrete wavelet packet transform (DWPT) are used to extract and study the dynamics of coherent structures in a turbulent rotating fluid. Three-dimensional turbulence is generated by strong pumping through tubes at the bottom of a rotating tank (48.4 cm high, 39.4 cm diameter). This flow evolves toward two-dimensional (2D) turbulence with increasing height in the tank. Particle image velocimetry measurements on the quasi-2D flow reveal many long-lived coherent vortices with a wide range of sizes. The vorticity field exhibits vortex creation, merger, scattering, and destruction. We separate the flow into a low-entropy "coherent" and a high-entropy "incoherent" component by thresholding the coefficients of the DWT and DWPT of the vorticity field. Similar thresholdings using the Fourier transform and JPEG compression together with the Okubo-Weiss criterion are also tested for comparison. We find that the DWT and DWPT yield similar results and are much more efficient at representing the total flow than a Fourier-based method. Only about 3% of the large-amplitude coefficients of the DWT and DWPT are necessary to represent the coherent component and preserve the vorticity probability distribution function (PDF), transport properties, and spatial and temporal correlations. The remaining small-amplitude coefficients represent the incoherent component, which has near Gaussian vorticity PDF, contains no coherent structures, rapidly loses correlation in time, and does not contribute significantly to the transport properties of the flow. This suggests that one can describe and simulate such turbulent flow using a relatively small number of wavelet or wavelet packet modes.

DOI: 10.1103/PhysRevE.72.016311 PACS number(s): 47.27.−i, 47.32.−y, 47.32.Cc

I. INTRODUCTION

Large-scale ordered coherent motions occur in a wide variety of turbulent flows despite existing in a rapidly fluctuating background turbulence [1,2]. These "coherent structures," which are associated with localized regions of concentrated vorticity, persist for times that are long compared to an eddy turnover time. The importance of coherent structures in turbulence has become recognized through the use of flow visualization. Examples of coherent structures identified in turbulent flows include hairpin vortices in boundary layer turbulence [3], plumes in turbulent convection, and vortices in turbulent shear flows. Coherent structures play a major role in the transport of mass and momentum, thus affecting transport, drag, and dissipation in turbulent flows. Due to their long lifetimes, coherent structures in the atmosphere strongly influence the exchange of heat, moisture, and nutrients between different locations. In industry, the prediction and control of transport, drag, and turbulence are important in many processes [4], and in some cases flows can be modified through the control of coherent structures [5,6].

The emergence of coherent vortices is especially striking in geostrophic turbulence, where the Coriolis force plays a dominant role [7,8]. Under the effect of rotation and stratification, geophysical flows develop large and robust coherent structures which can be identified and tracked for times much longer than their characteristic turnover time. Examples of such flows are high- and low-pressure systems, large vortical structures that are formed in the Gulf Stream meander, Mediterranean eddies (Meddies), and the Earth's jet stream; all can be observed and tracked by satellite imaging of the atmosphere or the ocean surface (e.g., see satellite imaging websites [9,10]). Large coherent structures are not limited to the Earth; the atmospheres of other planets also reveal structures such as Neptune's dark spot and Jupiter's zones, belts, and Great Red Spot.

Three-dimensional (3D) turbulence subjected to strong rotation develops columnar vortical structures aligned with the rotation axis, as observed in the present experiment and in previous laboratory experiments [11–14]. Correlation in this direction becomes large when the Coriolis force becomes large compared to inertial forces, and the flow proceeds toward a quasi-2D state. This two-dimensionalization allows energy to proceed toward larger scales through the inverse energy cascade and toward smaller scales through the forward enstrophy cascade [15], as observed in simulation [16–18] and experiments on rotating [12,13] and nonrotating quasi-2D flows [19]. The cascades of energy and enstrophy lead to a spontaneous appearance of intense localized coherent vortices containing most of the enstrophy of the flow. Vorticity filaments outside of those coherent structures are distorted and advected by the velocity field induced by the vortices. Thus, a rotating turbulent fluid flow can organize itself into large-scale coherent structures that are often long lived compared to dissipative time scales. The presence of long-lived coherent structures in turbulent rotating flow has been observed in both experiments [7,11–13] and simulations [17,18]. These structures are larger than the scale of the forcing. The large-scale coherent structures break the homogeneity of the flow and are thought to dominate the flow dynamics. The long lifetimes and spatial extent allow coher-

*Present address: The Racah Institute of Jerusalem, Israel.
†Electronic address: swinney@chaos.ph.utexas.edu

ent structures to play a significant active role in transport processes [20,21].

Due to the dynamical importance of coherent structures, any analysis of flow containing these structures should take into account their existence. One approach to analyze the coherent structures and the dynamics of such flow is to partition it into regions with different dynamical properties. Okubo [22] derived a criterion to separate flow into a region where strain dominates (hyperbolic region) and a region where vorticity dominates (elliptic region). The same criterion was later rederived by Weiss [23] and is now known as the Okubo-Weiss criterion. The criterion has been widely used to analyze numerical simulations of 2D turbulence. However, as pointed out by Basdevant and Philipovitch [24], the validity of the criterion's key assumption is restricted to the core of the vortices that correspond to the strongest elliptic regions. This limitation reduces the applicability of a decomposition using this criterion.

Another method that has been found useful in analyzing flow fields is proper orthogonal decomposition (POD). This projects a field onto a set of orthonormal basis functions where successive eigenvectors are obtained by numerically maximizing the amount of energy corresponding to that eigenmode [25]. (POD is known by other names, including the Karhunen-Loève decomposition, principal components analysis, and singular value decomposition; the basis functions are also known as empirical eigenfunctions and empirical orthogonal functions [25, p. 86].) Linear combinations of the basis functions ideally correspond to coherent structures in the flow. However, if the ensemble of fields is homogeneous, the basis functions become Fourier modes [25]. Furthermore, a single mode of the POD corresponds to a full field with structures in a particular spatial arrangement. If the structures in the field are not stationary, as in the case of our present flow, many modes will therefore be necessary to track the different spatial configurations. Indeed, application of POD to our data resulted in the extraction of the large-scale, low-amplitude mean flow structure of our field, rather than the continually moving intense coherent structures. We therefore do not include POD in this paper.

This paper separates a flow into coherent and incoherent components using wavelet transforms [26] to extract localized features at different spatial scales. The most important advantage of the wavelet representation over the more usual Fourier representation is the localization of the basis functions. A Fourier analysis is not well suited to pick out localized features such as intense vortices. The basis functions of a Fourier transform are localized in wave number space and hence spread out over the entire domain in physical space. The basis functions of the wavelet transform consist of dilations and translations of a "mother" wavelet, which contains multiple frequencies and has compact support (nonzero values only inside a finite interval) in physical space. The basis functions are well localized in both physical and wave number space; hence only a few coefficients suffice to describe localized features of a signal. The coefficients of the wavelet transform contain not only the amplitude but also the scale and position of the basis elements. Thus the coefficients can be used to track the size and location of features that are well correlated with the wavelet bases (e.g., [27,28]).

The discrete wavelet transform (DWT) [26] has been found to be well suited to analyze intermittent signals and systems containing localized features such as the intense vortices that occur in turbulence [29–31]. Farge and co-workers have extensively applied wavelets to the analysis and computation of turbulent flows [29–34].

The discrete wavelet *packet* transform (DWPT) [35] is a generalization of the DWT; the possible wavelet packet basis elements are a larger set which include spatial modulation of the wavelet basis. The advantage of the DWPT is that the choice of basis is adaptable to the signal to be analyzed.

Turbulent flow can be considered as a superposition of large-scale coherent motions, "fine-scale" incoherent turbulence, and a mean flow with interaction between the three constituents [36]. In numerical simulations of 2D turbulence [27,30,31], and more recently 3D turbulence [33], the coherent and incoherent turbulent background components have been separated using wavelet-based decompositions operating on the vorticity field. The coherent part, represented by only a small fraction of the coefficients, retained the total flow dynamics and statistical properties, while the incoherent part represented no significant contribution to the flow properties. This separation of the flow into two dynamically different components suggests that the computational complexity of turbulent flows could be reduced in simulations with coherent structures interacting with a statistically modeled incoherent background [31]. The application, however, has been heretofore primarily limited to results obtained from numerical simulations.

In this paper, we use the wavelet technique to analyze our particle image velocimetry (PIV) data on a rapidly rotating turbulent flow. Section II describes the experimental system. Section III describes the resulting flow fields obtained in the experiment. Section IV presents the techniques used to decompose the vorticity field into coherent and incoherent components. Section V presents the results obtained by applying the method to measurements on rotating turbulent flow. The conclusions are discussed in Section VI.

II. EXPERIMENT

A. Instrumentation and measurements

An acrylic cylinder (48.4 cm tall, 39.4 cm inner diameter) is fitted inside a square acrylic tank (40×40 cm^2 cross section, 60 cm tall) that has a transparent lid (Fig. 1) [37]. The tank is filled with distilled water at 24 ± 1 °C ($\rho=0.998$ g/cm^3, $\nu=9.5\times10^{-3}$ cm^2/s). The tank is mounted on a table that can be rotated up to 1.0 Hz.

Fluid is injected at the bottom of the tank by pumping water through a hexagonal array of tubes with grid spacing 2.3 cm; there are 192 sources and 61 sinks, as shown in Fig. 1. The source tubes are tee-shaped with a 2.5 cm shaft and 2.1 cm horizontal top (0.079 cm inside diameter) [see inset of Fig. 1(a)]. Each tee is screwed into the distributor. This design allows us to change the type of connector or change the forcing geometry by blocking or modifying sources or sinks. The tee source geometry was chosen to produce horizontal velocities and to minimize the vertical motions directly driven by the forcing. Further, the orientation of the

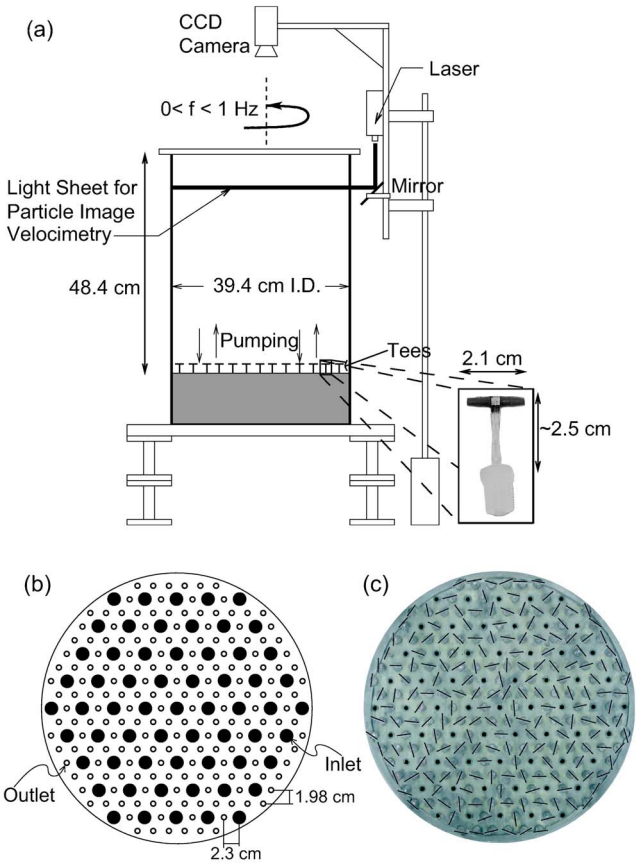

FIG. 1. (Color online) (a) A schematic of the apparatus. The height of the laser sheet is adjustable. Shown in the inset is a closeup of a single tee. (b) Horizontal cross section of the distribution of pumping sources (open circles) and sinks (black circles) (positions are to scale; see text for relative size of sources and sinks and tank diameter scale). (c) Overhead image of tank bottom, showing the tees. Overlaid are lines indicating the orientation of the tees.

tees was chosen to minimize cooperation between neighboring tees; however, it was not possible to eliminate completely a mean flow. The sinks are 1.27 cm diameter holes in the bottom of the distributor [Fig. 1(b)]. The forcing system is versatile and allows us to inject nearly homogeneous turbulence at a scale much smaller than the system size.

Flow rates can range up to 1400 cm^3/s, corresponding to flow velocities up to 8 m/s out of the tees. This corresponds to a Reynolds number of order 10^5 based on the jet velocity and the grid spacing of the tees. The Rossby number $U/2\Omega L$, based upon the same scales, is of order 50 near the bottom of the tank, near the forcing. However, the turbulence decays away from the forcing, with increasing height, and becomes more 2D due to the influence of rotation.

The data presented are for 0.4 Hz rotation rate and flow rate of 426 cm^3/s, producing 2.4 m/s velocity jets at the forcing tees. This corresponds to Reynolds and Rossby numbers of about 6×10^4 and 20, respectively, near the forcing. Near the top the rms flow velocity is about 2 cm/s and the maximal characteristic velocity length scale (twice the *e*-folding length of the velocity spatial correlation function) is about 5 cm; hence near the top the Reynolds number is about 1000. The Rossby number calculated from characteristic scales is 0.08, while the local averaged Rossby number calculated from the rms vorticity ($\omega_{rms}/2\Omega$) at such a flow condition is 0.3. The depth of our system thus allows us to observe more 3D (Rossby $\approx$20) or more 2D (Rossby $\approx$0.3) flow without changing control parameters, such as rotation or forcing.

The water is seeded with polystyrene ($\rho=1.067$ g/cm^3) spherical particles with diameters in the range 90–106 μm. The small mismatch in density results in a sedimentation terminal velocity of 4×10^{-2} cm/s in the absence of flow, which is insignificant compared to the measured flow velocities. The density mismatch also causes a lag in the response of the particles in regions of large acceleration [38,39]. We estimate the largest lag to be a 1% difference between the particle velocity and the flow velocity in the vortices at the top of the tank.

A 395 mW, 673 nm diode laser with attached light-sheet optics (from Lasiris) illuminates the particles in horizontal planes for flow visualization and PIV measurements. It is also possible to rotate the laser and optics by 90° to illuminate vertical planes for measurements of the vertical velocities. The thickness of the sheet is about 1 cm and varies less than 10% across the diameter of the tank. The laser is fixed to a carriage which allows us to adjust the vertical position of the light sheet without changing the pumping rate or system rotation rate.

Particles are imaged in the rotating frame with a charge-coupled device (CCD) camera (1004×1004 pixels, 30 frames per second) mounted 65 cm above the tank. The images are grabbed and stored into a memory buffer by a computer on the rotating table. A second, lower-resolution camera with an analog output allows us to view the flow when not grabbing digital images.

The laser pulses were timed so that pairs of pulses were imaged in successive frames of the CCD camera, which had a dead time of 120 μs between consecutive frames. The pulse duration was typically 10 ms with a 2 ms dark interval between pulses.

The analog signal from the second camera and power for the equipment on the table are sent through slip rings. The entire experiment is controlled remotely with a wireless ethernet connection and remote access software (PC ANYWHERE) by a computer in the nonrotating laboratory frame. This allows us to take multiple data sets, adjust the pumping rate, and adjust the position of the light sheet without having to stop the table.

To determine the two-dimensional projection of the velocity field we use a type of digital particle image velocimetry known as correlation image velocimetry (CIV) [40,41]. The CIV algorithm uses cross correlations over small interrogation regions between a pair of consecutive images to find particle displacements over known time intervals to obtain velocities. The CIV algorithm also allows for possible rotations and deformations of the interrogation region to take into account nonlinear particle motions in between images. The resulting velocity field is interpolated to a uniform regular grid by a cubic spline interpolation. The vorticity fields are calculated from the coefficients of the spline fit.

Our maximum data rate is 15 image pairs/s, which captures the dynamics of our flow. Images were taken for 20 *s*

periods, resulting in 300 fields in a sequence. Images were also taken at 30 *s* intervals (longer than measured decay time for our flow) over runs of 50 min, sufficient for convergence of statistical quantities. Resulting velocity and vorticity fields are on a 128×128 grid with a spatial resolution of 0.3 cm. We tested the CIV algorithm using simulated test particle images in known flow fields [42] and found that the velocity fields determined by the algorithm have about 2% rms error. Additional error results from perspective effects that cause apparent in-plane motions (e.g., see [43]). The error increases with distance from the optical axis and decreases for increasing object distance. The typical velocity (vorticity) error is about 15% (35%), but this error does not affect our data analysis.

B. Decay time

Characteristic decay times for our flow were measured by three different types of experiments. In each experiment, the measured decay time was taken as the *e*-folding relaxation time of the mean kinetic energy in the flow.

(i) Laminar (no forcing) *spin-down* experiments were conducted with the tees removed and replaced with a flat horizontal boundary. The tank was subjected to a sudden 10% decrease in rotation rate after the flow had reached solid-body rotation (no motion in the rotating tank frame). The predicted decay time of motions in laminar rotating flows with rigid, flat horizontal boundaries subject to small step changes in rotation is given by the Ekman dissipation time $\tau=H/(2\sqrt{\nu\Omega})$, where H is the depth of the fluid, ν is the kinematic viscosity, and $\Omega=2\pi f$ is the angular frequency of the container [44]. The corresponding decay time for the energy in the flow is $\tau=H/(4\sqrt{\nu\Omega})$. For our closed cylindrical tank without topography of depth $H=48.4$ cm, $\nu=0.095$ cm^2/s, and a rotation rate of 0.4 Hz, this gives a decay time of the energy as 78 s; the measured time was 64 s.

(ii) Laminar spin-down experiments were conducted in the same way as in (i), except that the tees were installed in the bottom of the tank. The characteristic decay time measured with the tees installed in the bottom of the tank for our flow was 18 ± 3 s. The reduced laminar spin-down time is due to the tees, which cause extra drag and secondary circulations that quickly bring the fluid to solid-body rotation.

(iii) Turbulent decay experiments were conducted by abruptly shutting off the forcing. For these experiments, the flow was allowed to reach a steady turbulent state (typically many decay times) under a constant pumping rate of 426 cm^3/s and rotation rate of 0.4 Hz before abruptly turning off the forcing. The measured decay time of 13 ± 3 s is long compared to the typical vortex turnover time of 1 s.

C. Passive scalar advection

To study the transport and mixing properties of our flow we examine numerically the motion of passive scalar point particles and passive scalar fields in the velocity fields obtained from the experiment. The velocity fields that we measure are a two-dimensional projection of a three-dimensional incompressible flow field. Therefore, they have a nonzero divergence and do not satisfy any fluid dynamical equation of motion. Nonetheless, they can give us useful information regarding the transport properties of the flow.

Initial locations are chosen for the point particles, and the positions of the particles are updated corresponding to the velocity fields such that $\mathbf{x}_{n+1}=\mathbf{u}_n\Delta t+\mathbf{x}_n$ where $\mathbf{x}_n$ is the position of the particle at time step n, and $\mathbf{u}_n$ is the velocity of the flow field at time step n at the location of the particle. Each velocity field is interpolated in space by a cubic spline to calculate the field at the location of a given particle. The time step Δt is chosen by the Courant condition [45], which avoids particles jumping over grid points or going too far at a given iteration. For our data this condition means $\Delta t<0.02<1/15$ s; therefore, fields must also be interpolated in time. The measured velocity fields vary slowly in time compared to our temporal resolution 1/15 s (measured correlation time is ≈2.4 s; see Sec. V A). We therefore justify the use of a cubic spline interpolation in time to achieve $\Delta t\ll1/15$ s (typically $\Delta t=0.001$ s).

We also examine the time evolution of a passive scalar field advected in the experimental velocity field by numerically integrating the advection-diffusion equation,

$$\frac{\partial c}{\partial t}=-\mathbf{u}\cdot\boldsymbol{\nabla}c+\kappa_D\nabla^2c, \tag{1}$$

where $c=c(\mathbf{x},t)$ is the passive scalar concentration and κ_D is a diffusion coefficient, chosen as necessary for numerical stability of the solution. The values of κ_D used correspond to Schmidt numbers (κ_D/ν) near 0.05. The numerical integration is performed using a pseudospectral method in polar coordinates based upon methods given in [46]. The grid is 128 Chebyshev modes in the radial direction and 128 Fourier modes in the azimuthal direction. The velocity field obtained by the CIV measurement is interpolated via a cubic spline onto the simulation grid. The numbers of radial and azimuthal modes were chosen so as to not underresolve our velocity fields on the nonuniform polar grid.

The singularity at the origin was avoided by choosing Chebyshev modes for the radial direction. The collocation points for Chebyshev modes have unit spacing on a circle, $x_i=\cos[\pi i/(N-1)]$, where x_i is the ith grid point, and N the total number of grid points. The grid points are clustered at the boundaries and sparse in the center of the domain. By defining the radial coordinate $r\in[-1,1]$ and using only the $r>0$ values, the radial grid points are sparse near $r=0$ and clustered at the boundary $r=R$. For an even number of modes the origin $r=0$ is skipped. However, the azimuthal grid is still dense at the origin, which requires us to use a very short time step $\Delta t\approx2\times10^{-4}$ s to avoid numerical instability. The experimentally determined velocity fields are then interpolated in time by the method described above for the tracer particle simulation.

The diffusive term is calculated implicitly by a Crank-Nicholson scheme, separately for the radial and azimuthal directions. The advection term is calculated explicitly by a predictor-corrector scheme using a third-order Adams-

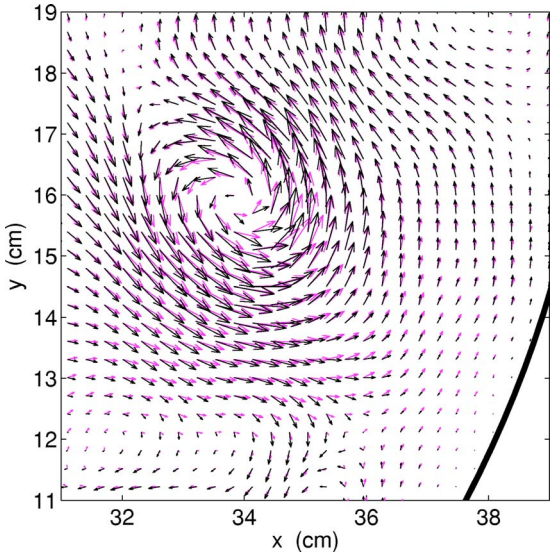

FIG. 2. (Color online) Closeup of a vortex in our tank near the boundary (bold line). The original field is represented by black vectors and the reconstructed field by light-colored vectors. The original and reconstructed fields are indistinguishable in the regions of uniform flow. The largest vectors correspond to 6.7 cm/s. The center of the tank is at $(x,y)=(19.2\ \text{cm}, 18.9\ \text{cm})$.

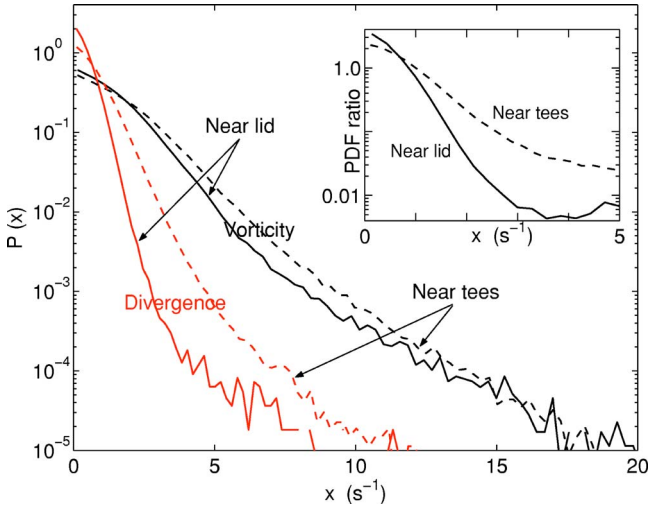

FIG. 3. (Color online) The PDF of the magnitude of vertical vorticity and divergence at two different heights in our tank, 4 cm below the lid (solid curves) and 10.4 cm above the top of the tees (dashed curves). Inset: the ratio of the divergence PDF to the vorticity PDF, showing the increase in the relative magnitude of the divergence near the forcing.

Bashforth step followed by a fourth-order Adams-Moulton step [45].

To perform the numerical analysis on the decomposed fields we construct a velocity field from a vorticity field. We make the assumption of 2D flow that the total vorticity is given by the measured vertical vorticity, $\omega=\omega_z$. We then use the 2D streamfunction-vorticity relation $\nabla^2\Psi=-\omega_z$ and solve Poisson's equation for the streamfunction Ψ using MATLAB's partial differential equation solver. The derivatives of the stream function are then used to calculate the velocity field by the relation $\nabla\times(\Psi\mathbf{z})=\mathbf{u}$, where $\mathbf{z}$ is the unit vector in the vertical direction.

The assumption above is clearly not valid close to the source tees, where the flow is 3D. However, close to the top of the tank the assumption becomes valid as the flow is quasi-2D. To test the reconstruction and the validity of the 2D approximation, we compare the original measured velocity fields to velocity fields reconstructed from the vorticity fields. A region of an original velocity field and the reconstructed field is shown in Fig. 2. The rms difference in the magnitudes of the original and reconstructed fields is about 2%. The reconstruction calculation does well in regions where there is a strong uniform flow. It does less well where there are large gradients in the velocity, in particular near vortices. However, on the whole the reconstructed velocity field follows the same behavior as the original field.

III. VELOCITY AND VORTICITY FIELDS

A. Transition to quasi-2D flow

Near the forcing sources (tees) at the bottom of the tank, the flow is very turbulent (Reynolds number $\approx 6\times 10^4$) and three dimensional (Rossby number $\gg 1$). However, moving vertically away and up the tank from the forcing, the turbulent velocities decay. The Reynolds number near the top of the tank where our data were collected is of order 1000 based upon the rms velocity of 2 cm/s and typical structure size of 5 cm (estimated from the velocity correlation function). The relative influence of rotation also becomes larger so that the Rossby number becomes about 0.3.

Figure 3 compares the magnitude of the divergence and vertical vorticity of the flow in our tank at two different heights. The divergence in our flow fields is small relative to the vorticity and 2Ω (≈ 5 rad/s). The divergence field consists of small length scales near the top and has a weak correlation with the vorticity field. The ratio of the rms divergence to the rms vorticity is 0.2, of the same order as the Rossby number. Near the bottom forcing, however, the divergence field becomes larger in amplitude and length scale, and more strongly correlates with structure in the vorticity field. The inset in Fig. 3 shows that the ratio of the divergence to vorticity increases near the forcing, where the flow is more 3D, and decreases near the top, where the flow is more 2D.

The particles in a plane near the top of the tank are confined primarily to the plane, and the particle streaks follow persistent coherent jets, cyclones (a vortex with rotation in the same sense as the tank), and anticyclones without crossing, similar to a 2D streamline flow [Figs. 4(a) and 4(b)]. In contrast, the motions of the particles near the bottom of the tank are much less organized; particles pass through the plane frequently and the particle streaks can cross and exhibit small fluctuations due to increased three-dimensionality and turbulence.

B. Persistent coherent structures

Localized coherent structures including large compact regions of intense vorticity and wispy filaments of intense vor-

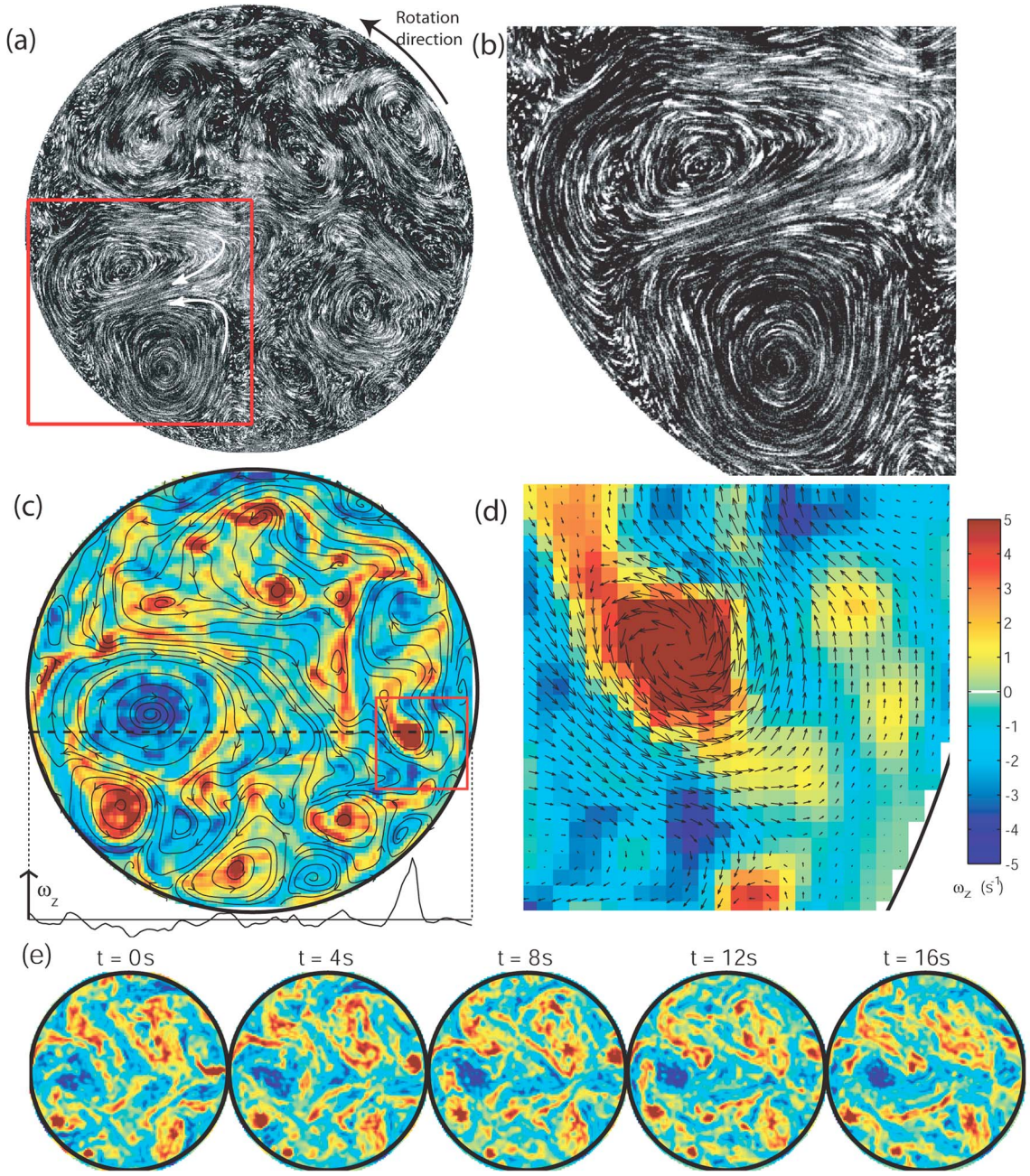

FIG. 4. (Color online) (a) Streak photo (400 ms exposure time) of the particle image fields in a horizontal plane 4 cm below the lid of the tank (see movie of tracer particles in our flow, #2 in [47]). (b) Closeup of the boxed region (18.7×18.7 cm^2) showing a cyclone (circular closed particle streaks) and an anticyclone (elliptical closed particle streaks to the upper left of the cyclone). (c) Vorticity field ω_z with the value along the dashed line shown in the trace below the field. The lines indicating the flow structure would be streamlines if the velocity field were divergence-free, which it is not. Arrows indicate flow direction. (d) Closeup of velocity and vorticity fields in an 8×8 cm^2 region near the boundary. The longest velocity vector corresponds to 6.7 cm/s. The vorticity is indicated by the gray (color) scale, where vorticity values are clipped at 5 s^{-1} to render visible weaker structures; the vorticity in the core of the strongest cyclone is 22 s^{-1}. (e) A sequence showing the time evolution of the vorticity field (see movie #4 in [47]).

ticity are evident in Figs. 4(c) and 4(d). We observe more cyclones (rotation in the same sense as the tank) than anticyclones, in accord with observations in previous experiments on rotating turbulent flows [12,13]. The amplitudes of vorticity at the core of the intense cyclones are typically more than ten times that of the surrounding flow [see Fig. 4(d) for a close-up of an intense cyclone]. The anticyclones, however, have a typical core vorticity amplitude only a few times that of the background.

The cyclones, anticyclones, and vorticity filaments are long lived and are active dynamically. The vortices and vortex filaments can be tracked by eye as the flow evolves in time [Fig. 4(e)]. Vortices are shed from the wall and travel across the tank and interact with one another. Vortex fila-

ments occasionally peel from vortices, advect with the flow, and sometimes roll up to form new vortices. Structures may disappear by merging with other structures or by stretching in a jet region between opposite sign vortices. Many of the small intense vortices with very short turnaround times (<1 s) exist on the order of a characteristic decay time (~ 10 s) before shearing apart or merging with neighboring structures.

Additionally, we see persistent structures such as the large cyclone and anticyclone that appear in Fig. 4. Such structures often appear in a preferred location in the tank. Presumably such preferred locations exist because of inhomogeneities in the forcing by the tees [cf. Fig. 1(c)]. A vortex can be kicked off its preferred location by a large perturbation when it interacts with neighboring vortices. If it begins to wander around the tank, it will generally disappear within a few characteristic decay times unless it returns to the preferred location. If a structure moves off its preferred location and disappears, a new structure will typically form, replacing the preexisting one within a few decay times. Some long-lived coherent structures occasionally persist throughout the entire duration of an experimental run (~ 5000 vortex turnover times). Further, we observe persistent structures as low as 5 cm above the tees. Observations closer to the tees are difficult because the three-dimensional turbulent flow rapidly moves particles into and out of the laser sheet.

A wide range of spatial scales is visible in the velocity and vorticity fields [Figs. 4(c) and 4(d)]. The largest features, approximately 10 cm in size, are coherent vortices that have a much larger amplitude than their surrounding region. There are also large-amplitude vortex filaments that stretch up to 10 cm; these can be as thin as the grid resolution in the transverse direction. Small-scale persistent structures less than 1 cm in size yet large in amplitude are also observed. The region between the various large-amplitude coherent structures is occupied by relatively low-amplitude vorticity [see the vorticity trace in Fig. 4(c)].

IV. DECOMPOSITION OF THE VORTICITY FIELD

A. Wavelets and wavelet packets

The discrete wavelet transform is a multiresolution analysis that successively decomposes the signal into coefficients that encode coarse and fine details at successively lower resolution [35]. The basis elements of the transform $\psi_{s,p}$ correspond to dilations and translations of a mother wavelet function ψ, where s is the scale (dilations) of the wavelet and p its position (translations). Successive levels of the transform continue to split the coarse detail coefficients, effectively analyzing the signal at coarser and coarser resolution.

The discrete wavelet packet transform is a generalization of the discrete wavelet transform. The basis elements of the wavelet packet transform include, in addition to dilations and translations, spatial modulation of the mother wavelet at different resolutions. The basis elements $\psi_{s,p,k}$ take on an additional parameter k, which roughly corresponds to the modulation of the wavelet packet. In contrast to the DWT, the choice of basis of the DWPT is not unique [26]. The wavelet basis is contained within the possible choices of wavelet packet bases. To select the particular basis to use, a natural choice is the wavelet packet basis in which the coefficients of the transform most efficiently represent the signal. This is known as the "best basis." The best basis is typically calculated based upon the minimization of an effective entropy measure of the coefficients [35], thus minimizing the "information cost" of the coefficients in the best basis. The flexibility in basis choice of the DWPT allows the transform to adapt the basis to the particular signal being analyzed. For example, if the signal contains regions of rapid fluctuations, the basis choice will reflect that by including more basis elements with high modulation.

We use the DWT [$O(N)$ operations] and DWPT [$O(N \log_2 N)$ operations] on our experimentally obtained vorticity fields, as previous authors have done using 2D turbulent flow data from numerical simulations in a periodic square domain (e.g., [27,30,31]). We use the MATLAB wavelet toolbox and the coiflet 12 (coif2 in MATLAB notation) as the analyzing wavelet. The coiflet family of wavelets (see Ref. [26], p. 258) both has compact support and can generate an orthogonal basis. These two properties allow one to select the localized features of the coherent structures and to treat the decomposition of the vorticity field as two orthogonal components. The choice of wavelet does not alter the results significantly as long as the basis is sufficiently smooth [31].

B. Coherent structure extraction

We use an algorithm for coherent structure extraction based upon a denoising algorithm (e.g., Chap. 11 of Ref. [35]). In the denoising, the assumption is that the original signal can be represented by a few large-amplitude coefficients of an orthogonal transform using an appropriate set of basis functions, while the noise is contained in the many remaining coefficients of small amplitude. The denoising is then performed by applying a threshold to the resulting coefficients of the transform. Coefficients above the threshold amplitude are assumed to correspond to the signal while coefficients below the threshold correspond to the "noise." The few large-amplitude coefficients are called the "coherent" coefficients, while the many small-amplitude coefficients are "incoherent." The coherent and incoherent parts of the vorticity are then reconstructed by the inverse transform.

The choice of the threshold separating the coherent and incoherent parts of the signal is based upon a measure of the number of significant coefficients N_0, which is the theoretical dimension of the signal, defined by

$$N_0(f) = e^{H(f)} \tag{2}$$

where $H(f)$ is the entropy of a discrete signal $f=[f_i]$ (where $[f_i]$ is the set of discrete values of an arbitrary signal f). In our case, the f_i's correspond to the discrete values of our vertical vorticity measurements. The entropy $H(f)$ is defined as

$$H(f) = -\sum_{i=1}^{N} p_i \ln p_i \tag{3}$$

where $p_i = |f_i|^2 / \|f\|^2$ is the normalized square modulus of the ith element of the signal, with N the number of elements and

$\|f\|^2=\Sigma_i|f_i|^2$. N_0 indicates how many of the largest coefficients should be retained to give an efficient, low-entropy, representation of the signal.

Thus, the decomposition algorithm is the following. We take the transform of an individual measured vorticity field. For the DWPT, the best basis is used. Then we find the number of significant coefficients N_0 of the transformed vorticity field in the transform basis. The threshold is therefore based upon the value of the N_0^{th} largest coefficient. Coefficients whose modulus is larger (smaller) than the threshold correspond to the coherent (incoherent) part of the vorticity field. We then take the inverse transform to get the coherent part in physical space. The incoherent field is reconstructed by subtracting the coherent from the total field. The process is then repeated for each of our vorticity fields. Our algorithm contains no adjustable parameters other than the selected wavelet and is based upon the assumption that the flow field has a low-entropy component, corresponding to the coherent structures, and a high-entropy component, corresponding to an incoherent background.

Our algorithm is different from the various iterative algorithms of Farge *et al.* [31] and others [27,35]. In the denoising algorithm described in [27,35], successive iterations extract a fraction of the coherent coefficients until a stopping criterion is met. The fraction of retained coefficients at each step and the stopping criterion are adjustable parameters. However, the basis of the DWPT can change at each iteration. The number of coefficients retained therefore loses its meaning since coefficients can be selected from completely different bases. Therefore, we only perform a single iteration without changing the basis for the DWPT. In the algorithm of Farge *et al.* [31], an *a priori* assumption is made of a Gaussian white noise incoherent component superimposed upon a non-Gaussian component of coherent vortices. The threshold is then iteratively found to separate the two without adjustable parameters.

C. Fast fourier transform, JPEG compression, and Okubo-Weiss-based techniques

To examine the relative efficiency of the wavelet-based decompositions, we compare the DWPT and DWT to three other algorithms; one based upon a Fourier transform, a second on basic JPEG compression, and a third on the method developed by Okubo [22] and Weiss [23].

For the Fourier transform algorithm we threshold the coefficients of a two-dimensional fast Fourier transform (FFT) of our vorticity. The coherent fields are then constructed via an inverse FFT of the largest-amplitude coefficients. The incoherent remainder fields are constructed by subtracting the coherent fields from the original fields.

The basic JPEG algorithm consists of subdividing an image into 8×8 blocks and taking the discrete cosine transform over the sub-blocks. The coefficients are arranged based upon the global average of the amplitudes among the sub-blocks. The average of the amplitudes is used to determine which modes to keep. After the threshold, each sub-block retains the same number of modes, each in the same position. Thus the number of modes retained must be a multiple of the number of sub-blocks which compose the image (for our 128×128 fields, this is 256). For more information on the JPEG image compression standard see Ref [48], Chap. 3.

The Okubo-Weiss criterion splits the fields into elliptic and hyperbolic regions, dominated by vorticity and strain, respectively. The regions dominated by vorticity and strain are then separated and taken to be the coherent and incoherent fields. For details on the Okubo-Weiss criterion see Ref. [24].

V. RESULTS

A. Decomposed vorticity fields

The resulting coherent and incoherent vorticity fields obtained from the wavelet packet, wavelet, Fourier, and JPEG techniques are compared in Fig. 5. The Okubo-Weiss criterion was also tested for comparison with the other decomposition methods. The fields shown are constructed with the same number of coefficients for the DWPT, DWT, and Fourier transforms, and the closest approximate number for JPEG.

The coherent fields in Fig. 5 appear to retain the large scale coherent structures [cf. Figs. 4(c) and 4(e)]. The DWPT, DWT, and Fourier methods preserve the structure of the total vorticity field. The Okubo-Weiss criterion excises primarily the regions of large-amplitude vorticity, which generally correspond to the cores of vortices. However, it ex-

TABLE I. Statistical properties of the decomposed vorticity fields using entropy criterion.

		Decomposition									
		Wavelet packet		Wavelet		Fourier		JPEG		Okubo-Weiss	
Quantity	Total	Coherent	Incoherent	Coherent	Incoherent	Coherent	Incoherent	Coherent	Incoherent	Coherent	Incoherent
Coefficients retained (%)	100	2.4	97.6	2.7	97.3	4.1	95.9	13.1	86.9	40.2	59.8
Enstrophy/field ($s^{-2}\times 10^4$)	4.33	3.63	0.63	3.67	0.62	3.68	0.56	2.92	1.33	3.21	1.12
Vorticity skewness	0.78	0.80	0.02	0.85	0.04	0.62	0.20	0.53	0.24	1.22	–0.07
Vorticity kurtosis	7.09	7.03	3.88	7.58	3.42	5.37	7.85	5.27	6.55	11.81	8.28

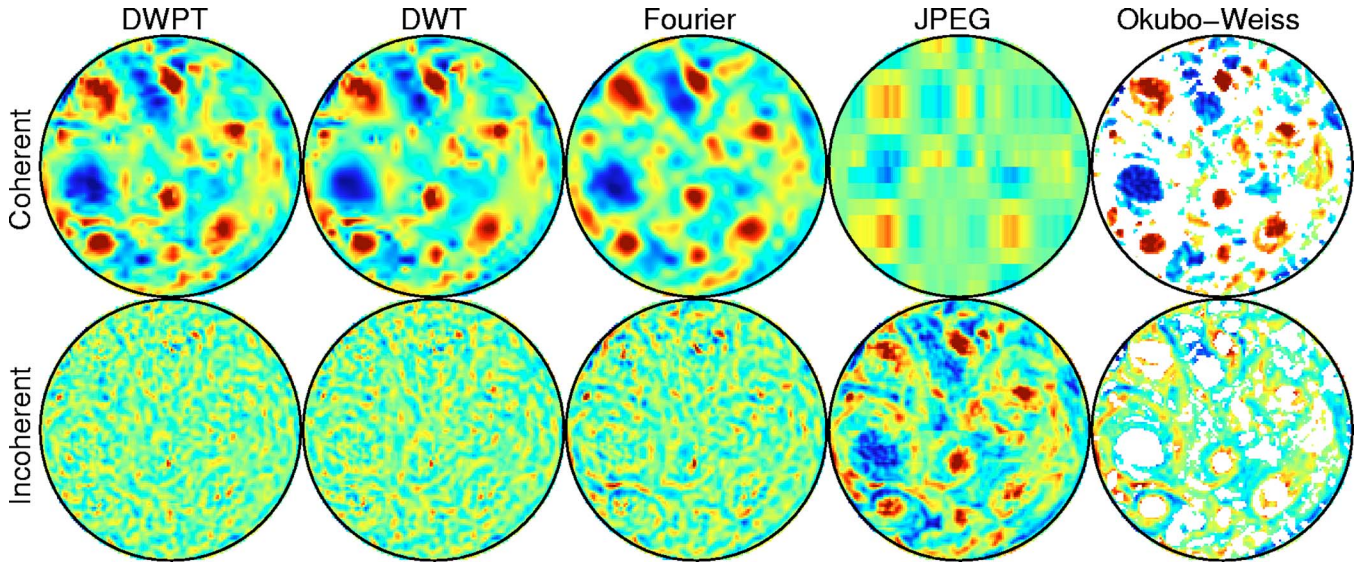

FIG. 5. (Color online) Decomposed vorticity fields, all for the same number of coefficients (2.4%) retained in the coherent fields (except for Okubo-Weiss method and approximate for JPEG method). Top row: coherent fields. Bottom row: incoherent fields. See movie comparing the time evolution of the coherent and incoherent fields produced by the various extraction methods, #1 in [47].

tracts only the cores and leaves behind the peripheries. The JPEG does poorly with so few coefficients; it barely picks out some of the stronger vortices in the field.

For the same number of coefficients, 2.4%, the DWPT and DWT do a better job of extracting structure in the fields than the Fourier decomposition, which leaves more structure behind in the incoherent field (Fig. 5, movie #1 in Ref. [47]). The JPEG incoherent field is large amplitude because of the few coefficients retained in the coherent field. The incoherent fields resulting from the DWPT, DWT, and the Fourier transform are mostly devoid of large-scale structures and are much smaller in amplitude. The incoherent fields are also poorly correlated in time and are devoid of large scale structures or any other feature which can be tracked by eye (Fig. 5 and associated movie).

The Okubo-Weiss criterion selects the centers of the vortices where vorticity dominates strain. This accounts for a large portion of the enstrophy. It extracts about 74% of the enstrophy in the vorticity dominated regions, which cover about 40% (not coefficients) of the flow. However, the method leaves behind holes in the vorticity field that act as coherent structures and are often surrounded by large values of vorticity. The resulting "incoherent" field thus retains coherent properties. The Okubo-Weiss criterion also does poorly in recovering the statistics of the total field, as shown in Table I. Furthermore, the decomposition shown in Fig. 5 was performed without regard to the Okubo-Weiss validity criterion, which restricts the application of the criterion to the very centers of the vortices or regions of very large vorticity [24]. If the validity criterion is applied, much less is retained in the coherent field, and the incoherent field ends up with large values of vorticity.

Statistical properties of the decompositions are shown in Tables I and II. Table I lists the results from setting the threshold of the various transforms based upon the number of significant coefficients calculated from Eq. (2). On average about 2–3 % of the large-amplitude coefficients of the wavelet-based decompositions were retained in the coherent fields, which account for about 85% of the total enstrophy of the flow. The Fourier retains roughly the same enstrophy but requires more coefficients, about 4%. The JPEG decomposition retains only 67% of the total enstrophy with about 13% of the large-amplitude coefficients.

Owing to the compact support of their basis functions, fewer coefficients were needed for the DWPT and DWT, based upon the entropy criterion in Eq. (3), than for the Fou-

TABLE II. Statistical properties of the decomposed vorticity fields retaining the same number of coefficients, 2.4%, as the DWPT decomposition (approximate for JPEG method).

		Decomposition							
		Wavelet packet		Wavelet		Fourier		JPEG	
Quantity	Total	Coherent	Incoherent	Coherent	Incoherent	Coherent	Incoherent	Coherent	Incoherent
Coefficients retained (%)	100	2.4	97.6	2.4	97.6	2.4	97.6	3.0	97.0
Enstrophy/field ($s^{-2} \times 10^4$)	4.33	3.63	0.63	3.60	0.69	3.28	0.92	0.96	3.18
Vorticity skewness	0.78	0.80	0.02	0.86	0.04	0.51	0.32	0.06	0.72
Vorticity kurtosis	7.09	7.03	3.88	7.62	3.47	4.77	7.85	4.84	7.08

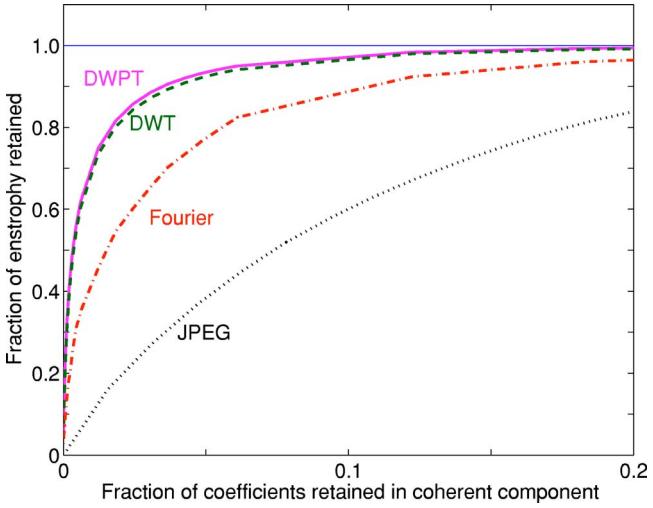

FIG. 6. (Color online) The percent enstrophy retained in the largest-amplitude coefficients as a function of the number of coefficients kept. In order from best (most efficient) to worst: wavelet packet, wavelet, Fourier, JPEG results.

rier and JPEG decompositions. Compression curves for the enstrophy of the various decompositions applied to our vorticity fields are shown in Fig. 6. The DWPT and DWT both do similarly well at extracting the enstrophy in the fields with only a small number of coefficients. The DWPT probably does slightly better due to the adaptability of its basis. The Fourier-based methods do not converge as rapidly as the wavelet-based methods. This is likely due to the nonlocality of the basis functions when applied to a field which has localized structures and sharp features.

The wavelet-based algorithms also do a better job preserving the skewness and kurtosis of the total vorticity in the coherent component, while the incoherent components are much closer to a Gaussian distribution (skewness 0, kurtosis 3). Table II displays the results from setting the threshold on the transforms so that each method retains 2.4% of the coefficients in the coherent component (since the JPEG coefficients must be a multiple of the number of 8×8 blocks, 256, this restriction is relaxed). For the same number of retained coefficients, the DWT and DWPT clearly outperform the Fourier method in terms of preserving the statistics of the total vorticity field.

Figure 7 shows that the coherent fields from the wavelet packet and wavelet decompositions rapidly converge to the statistics of the total vorticity field. The coherent fields preserve the non-Gaussianity of the vorticity probability distribution function (PDF) without having to extract many coefficients. The respective incoherent fields also rapidly converge to Gaussian statistics. This suggests that wavelets and wavelet packets do a good job of extracting the coherent structures from the vorticity field. The near-Gaussianity of the incoherent field suggest that the transforms have left the remainder without coherent structure.

The coherent components of the Fourier and JPEG decompositions, however, converge to the statistics of the total fields much more slowly. To obtain the same level of fidelity, both the Fourier and JPEG decomposition must extract many

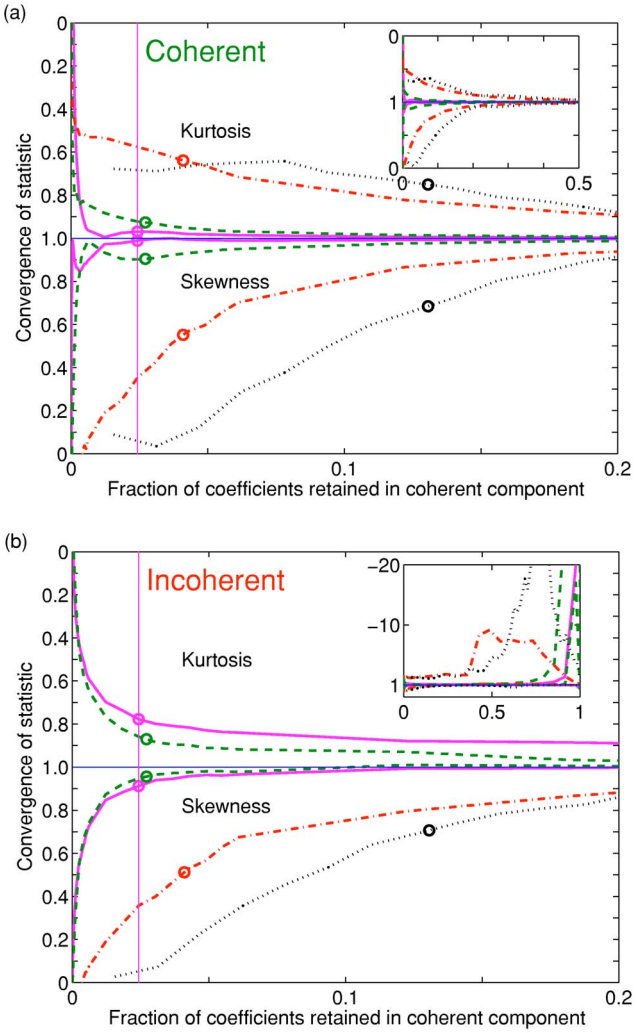

FIG. 7. (Color online) Convergence of the skewness and kurtosis of the vorticity PDFs for the various decompositions, plotted with quantities defined so that they approach unity as they converge. The vertical line indicates the fraction of coefficients retained in the wavelet packet decomposition. (a) Convergence of the coherent component. Plotted: kurtosis ratio $|k_{\mathrm{coh}}/k_{\mathrm{total}}|$; skewness ratio $|s_{\mathrm{coh}}/s_{\mathrm{total}}|$. (b) Convergence of the incoherent component. Plotted: kurtosis ratio $2-k_{\mathrm{incoh}}/3$; skewness ratio $1-|s_{\mathrm{incoh}}/s_{\mathrm{total}}|$. Note that unity on the graph represents the respective statistic for a Gaussian distribution: skewness 0, kurtosis 3. The kurtosis of the Fourier and JPEG incoherent fields is large and off the main plot. The insets show the convergence behavior at large numbers of retained coefficients. The open circles on the curves correspond to the fraction of coefficients retained for the corresponding techniques using the entropy criterion as a threshold.

more coefficients. This inefficiency results in overtransformed fields. Further, the insets in Fig. 7(b) show that the kurtosis of the incoherent component never converges to anything small, but increasingly deviates from Gaussian. This suggests that the Fourier decomposition is not separating the coherent structures from the background.

The probability distribution function of vorticity has broad wings (Fig. 8), which correspond to the large vorticity values that occur in the coherent vortices and vorticity fila-

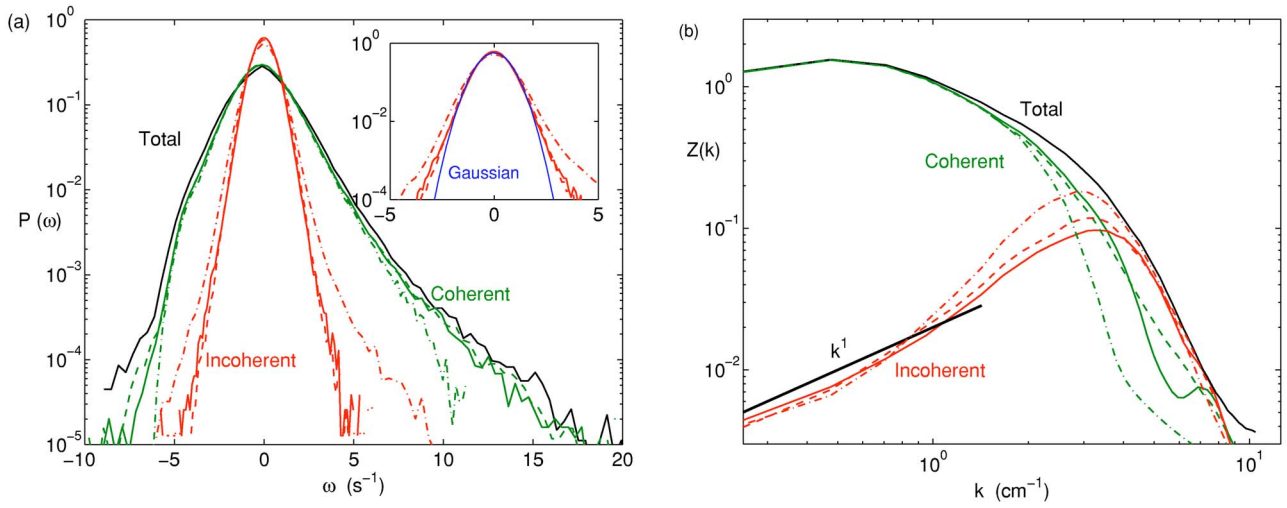

FIG. 8. (Color online) (a) Vorticity PDFs of the total, coherent, and incoherent fields, where the inset shows the incoherent PDFs plotted together with a Gaussian fit to the wavelet packet results. (b) Enstrophy spectra $Z(k)$ of total, coherent, and incoherent fields, calculated on a square subsection of our circular domain. The solid, dashed, and dash-dotted lines correspond to the wavelet packet, wavelet, and Fourier decompositions, respectively. The k^1 line is the spectral slope for Gaussian white noise in 2D. The wave number is defined as $k=2\pi/L$.

ments. The preference for cyclonic (positive vorticity) structures over anticyclonic structures appears as a large positive skewness (see also Table I or II). While the PDFs for the DWPT and DWT coherent vorticity fields are nearly the same as that for the total vorticity field, the PDF for the corresponding incoherent field is narrower and more symmetric, indicating the lack of high-intensity structures.

Consider the enstrophy spectrum of the vorticity fields, as shown in Fig. 8(b). It is clear from the enstrophy spectra of the total field that most of the enstrophy is contained in long wavelengths (small k). This agrees well with the observation of the vorticity fields and the dominance of large structures with large-amplitude vorticity. The enstrophy spectrum, shown in Fig. 8, does not contain a well-defined scaling region corresponding to a cascade of enstrophy. A cascade would not be expected for our quasi-2D flow, which is forced by the broadband 3D turbulence in the bottom of the tank rather than by injection of energy at a single well-defined wave number. The presence of large structures which extend well into the 3D region alone tells us that we must have a broad spectrum energy injection.

The coherent field contains the same large structures that are present in the total field. Accordingly, the enstrophy spectrum of the coherent field matches that of the total field at long wavelength [Fig. 8(b)]. The incoherent field contains negligible enstrophy at large scales, indicating the lack of large-scale features. This is apparent in the vorticity decomposition (see Fig. 5). The incoherent field has only small structures and is the dominant contribution to the enstrophy at large k.

The wavelet-based and Fourier decompositions also retain the spatial and temporal correlations in the coherent field, as Fig. 9 illustrates with the DWPT and DWT yielding almost the same results. The long-time correlation is in part due to

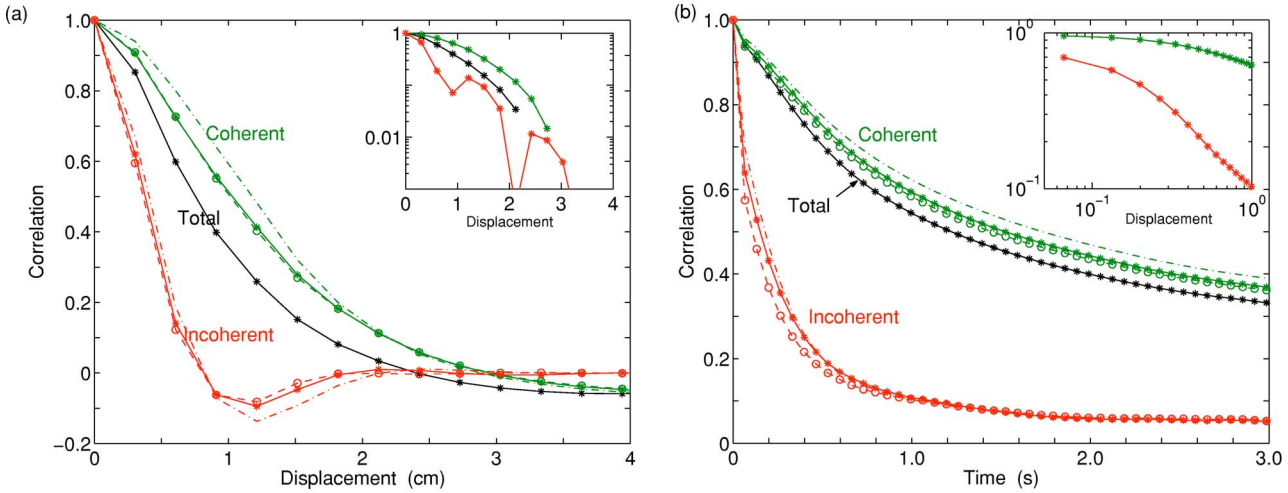

FIG. 9. (Color online) (a) Space and (b) time correlations of the decomposed vorticity fields. The solid, dashed, and dash-dotted curves correspond to the DWPT, DWT, and Fourier decompositions.

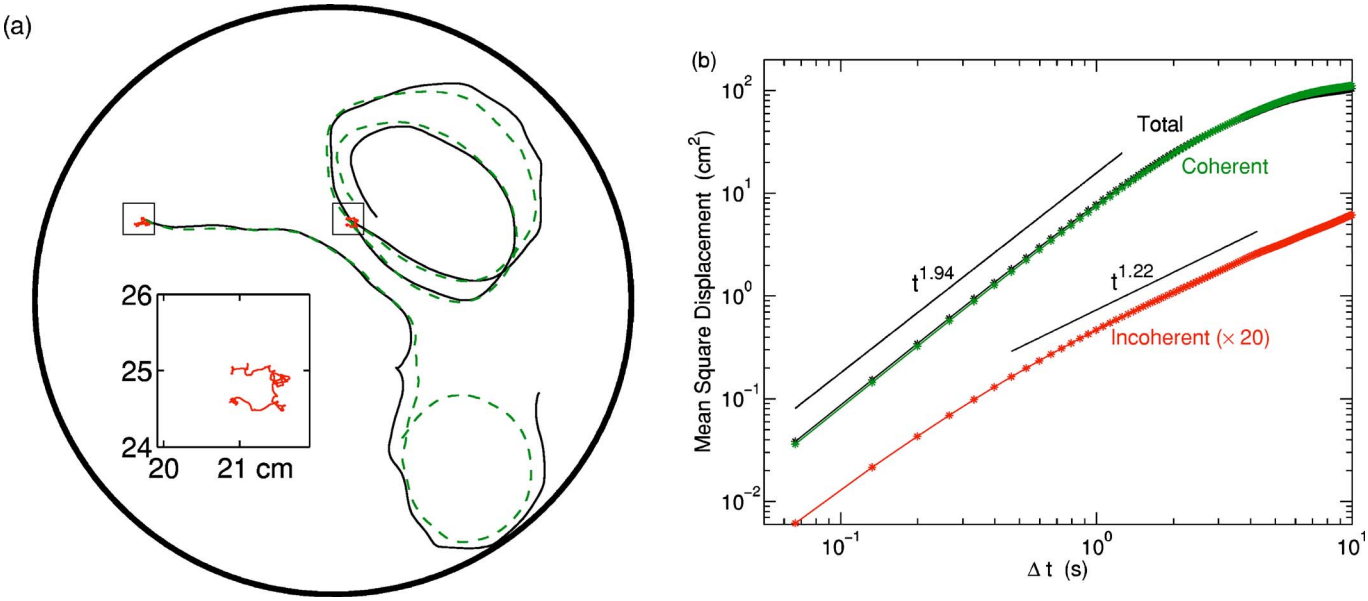

FIG. 10. (Color online) (a) Simulated paths of numerical tracer particles in the total field (solid curves) and in the coherent (dashed curves) and incoherent field (boxed regions) for the DWPT (total time 20 s). The inset shows an expanded view of a path in the incoherent field. (b) Mean squared displacements for the tracers in the total, coherent, and incoherent velocity fields. The exponents for the total and coherent fields are 1.94 while for the incoherent remainder the exponent is 1.22 over the range indicated. Both results are for the wavelet packet.

the presence of long-lived coherent structures. In contrast, for the incoherent field the spatial and temporal correlations are short ranged, indicating the absence of large-scale and long-lived structures.

B. Transport of passive scalar particles and concentration fields

Paths computed for some passive scalar "particles" in the measured velocity fields are shown in Fig. 10(a). Over the 20 s duration of the measurement, the particles are advected around a large portion of the tank. The motion of the particles depends on their location in the flow. For example, a particle can spend time caught in a vortex, following the motion of the vortex as it meanders slowly in a localized region of the tank [path in upper right of Fig. 10(a)]. Occasionally the particle will escape from a vortex and then be carried by a high-velocity jet, which can transport a particle large distances in a short time. A particle may then be captured by a vortex [e.g., path ending in lower right of Fig. 10(a)].

The resulting mean squared displacement of the tracer particles in the velocity fields obtained by experiment is shown in Fig. 10(b). It exhibits approximately t^2 scaling at short times, which looks "flightlike" [21]. At long times the finite size of the tank becomes significant and the scaling exponent becomes smaller.

Both the wavelet and wavelet packet coherent fields disperse the tracer particles similarly around the tank; the scaling behavior of the mean squared displacement is also the same. Differences in the paths are due to the sensitive dependence upon initial conditions of a turbulent flow field.

We find a striking difference in the behavior of a numerically integrated passive scalar particle in the coherent and incoherent fields. The incoherent fields make no significant contribution to the transport properties; rather, particles are confined to a small region, as shown in the inset in Fig. 10(a). This is due to the rapid decorrelation in time of the incoherent fields. The rapid fluctuations cause the tracers to jiggle around and the scaling of the mean squared displacement of the tracers in the incoherent fields approaches that of a random walk.

The evolution of a passive scalar field in the measured velocity field is similar to that for tracer particles. Results for the coherent and incoherent fields produced by the DWPT are shown in Fig. 11, which illustrates the stretching and folding; the results for the total field are similar to that of the coherent field. By 4 s the scalar has already been significantly stretched by the velocity fields. There is no significant advection in the incoherent fields and this is similar to results obtained with pure diffusion (no advection term). This is expected from the short time and space correlations of the incoherent fields (Fig. 9). Similar results were obtained for the DWT and Fourier methods. Our results agree well with those of Beta *et al.* [34] who, using the DWT, found that the coherent field is responsible for the mixing in a numerically simulated 2D turbulent flow.

VI. DISCUSSION

We find that flow which is strongly forced near the bottom of a deep rapidly rotating tank evolves with increasing height in the tank from 3D turbulence into rotation-dominated turbulence. This is due to the competition between the turbulent forcing, which is 3D, and the rotation, which tends to two-

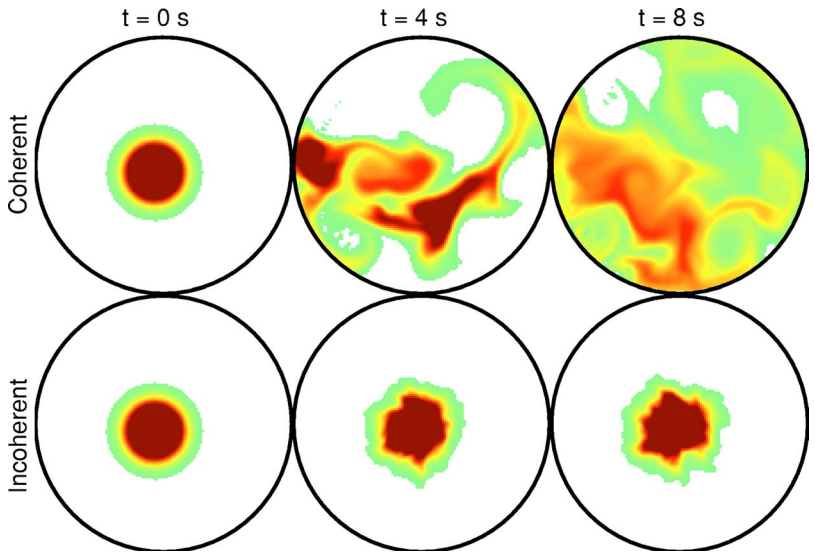

FIG. 11. (Color online) Advection of a passive scalar field in the velocity field of the DWPT, as computed from the advection-diffusion equation (1). By 8 s the scalar field has been significantly mixed by the coherent field, while it appears only to have been diffused in the incoherent field. (See movie of the evolution of a numerically integrated passive scalar in the coherent and incoherent field, #3 in [47]).

dimensionalize the flow. Near the forcing the turbulent velocities are large and the flow is 3D. Away from the forcing the spatial decay of turbulence allows the rotation to become increasingly important with increasing height. Motions of the particles in the flow are more organized in the horizontal plane near the top, consistent with two-dimensional columnar vortices. The flow in the rotationally dominated (Rossby number ≈ 0.3) region of our tank has a strongly non-Gaussian vorticity PDF and exhibits properties of 2D turbulence, such as large-scale long-lived coherent vortices, vortex filamentation, and merger.

The vertical component of vorticity describes the flow well near the top where the flow is quasi-2D as a consequence of the rotation. We are thus able to use the projected flow field as measured in a horizontal plane for analysis with wavelet- and Fourier-based decompositions. We have shown that wavelet-based transforms can be used to separate the coherent structure-containing quasi-2D turbulent flow into a non-Gaussian coherent component represented by as few as 3% of the large-amplitude, low-entropy coefficients of the transform and a nearly Gaussian incoherent component, represented by the remaining small-amplitude, high-entropy coefficients. We are able to obtain this result without an *a priori* assumption of Gaussianity or non-Gaussianity of the two components.

The discrete wavelet packet transform and the discrete wavelet transform yield very similar results, despite the adaptability of the DWPT basis. The DWT is therefore made preferable by its faster computation [$O(N)$ versus $O(N \log_2 N)$ operations].

Because our flow fields contain compact structures, the localized basis functions of the DWPT and DWT outperform Fourier and JPEG decompositions. Both the DWPT and DWT have more rapid convergence of the statistics of the extracted coherent component toward that of the total flow. The rapid convergence of the skewness and kurtosis of the vorticity PDF suggest that the wavelet-based methods have efficiently captured the coherent structures. The Fourier and JPEG results converge much more slowly and are thus unable to efficiently capture the large higher moments of the vorticity PDF. This suggests that the Fourier and JPEG methods have not really extracted the coherent structures despite the appealingly smooth visual appearance of the structures in the coherent field of the Fourier transform. Indeed, the superior performance of the DWT over the JPEG is exploited by the emerging next generation JPEG2000 image compression standard, which uses a biorthogonal DWT [48,49]. The incoherent remainder of both the DWPT and DWT converge rapidly toward Gaussian statistics, while incoherent remainders of the Fourier and JPEG methods do not converge to any value.

The coherent components of the DWPT and DWT retain all of the properties of the total field, including the large-scale structures, shape of the vorticity PDF, long spatial and temporal correlations, and transport properties. Further, the coherent component retains the large skewness and kurtosis of the total field. In contrast, the incoherent remainder has only small-scale short-lived features and does not contribute significantly to the transport. Thus in analysis of flow dynamics and transport, it may be sufficient only to consider the coherent component. These results suggest that it is reasonable to reduce the computational complexity of turbulent flows by considering only the low-dimensional coherent structures, which interact with a statistically modeled incoherent background.

ACKNOWLEDGMENTS

We thank Bruno Forisser and Emilie Regul for assistance in the initial implementation of the Okubo-Weiss criterion and wavelet analysis, respectively. We thank Kenneth Ball, Carsten Beta, Ingrid Daubechies, Marie Farge, Philip Marcus, Kai Schneider, and Jeffrey Weiss for helpful discussions. This research was supported by the Office of Naval Research.

[1] A. K. M. F. Hussain, J. Fluid Mech. **173**, 303 (1986).
[2] K. R. Sreenivasan, Rev. Mod. Phys. **71**, S383 (1999).
[3] S. K. Robinson, Annu. Rev. Fluid Mech. **23**, 601 (1991).
[4] J. C. R. Hunt, Annu. Rev. Fluid Mech. **23**, 1 (1991).
[5] J. T. C. Liu, Annu. Rev. Fluid Mech. **21**, 285 (1989).
[6] J. Lumley and P. Blossy, Annu. Rev. Fluid Mech. **30**, 311 (1998).
[7] J. Sommeria, S. D. Meyers, and H. L. Swinney, Nature (London) **331**, 689 (1988).
[8] J. C. McWilliams, J. Fluid Mech. **146**, 21 (1984).
[9] NOAA/NESDIS interactive GOES archive, available at http://wist.ngdc.noaa.gov/wist/goes.html
[10] http://visibleearth.nasa.gov/
[11] A. D. McEwan, Nature (London) **260**, 126 (1976).
[12] A. Colin de Verdiere, Geophys. Astrophys. Fluid Dyn. **15**, 213 (1980).
[13] E. J. Hopfinger, F. K. Browand, and Y. Gagne, J. Fluid Mech. **125**, 505 (1982).
[14] S. C. Dickinson and R. R. Long, J. Fluid Mech. **126**, 315 (1983).
[15] R. H. Kraichnan, Phys. Fluids **10**, 1417 (1967).
[16] L. M. Smith, J. R. Chasnov, and F. Waleffe, Phys. Rev. Lett. **77**, 2467 (1996).
[17] L. M. Smith and F. Waleffe, Phys. Fluids **11**, 1608 (1999).
[18] F. S. Godeferd and L. Lollini, J. Fluid Mech. **393**, 257 (1999).
[19] J. Paret and P. Tabeling, Phys. Rev. Lett. **79**, 4162 (1997).
[20] A. Provenzale, Annu. Rev. Fluid Mech. **31**, 55 (1999).
[21] T. H. Solomon, E. R. Weeks, and H. L. Swinney, Phys. Rev. Lett. **71**, 3975 (1993).
[22] A. Okubo, Deep-Sea Res. Oceanogr. Abstr. **17**, 445 (1970).
[23] J. Weiss, Physica D **48**, 273 (1991).
[24] C. Basdevant and T. Philipovitch, Physica D **73**, 17 (1994).
[25] P. Holmes, J. L. Lumley, and G. Berkooz, *Turbulence, Coherent Structure, Dynamical Systems and Symmetry* (Cambridge University Press, New York, 1996), Chap. 3.
[26] I. Daubechies, *Ten Lectures on Wavelets* (SIAM, Philadelphia, 1992).
[27] A. Siegel and J. B. Weiss, Phys. Fluids **9**, 1988 (1997).
[28] C. Schram and M. L. Riethmuller, Meas. Sci. Technol. **12**, 1413 (2001).
[29] M. Farge, Annu. Rev. Fluid Mech. **24**, 395 (1992).
[30] M. Farge, E. Goirand, Y. Meyer, F. Pascal, and M. V. Wickerhauser, Fluid Dyn. Res. **10**, 229 (1992).
[31] M. Farge, K. Schneider, and N. Kevlahan, Phys. Fluids **11**, 2187 (1999).
[32] M. Farge, http://wavelets.ens.fr/
[33] M. Farge, K. Schneider, G. Pellegrino, A. A. Wray, and R. S. Rogallo, Phys. Fluids **15**, 2886 (2003).
[34] C. Beta, K. Schneider, M. Farge, and H. Bockhorn, Chem. Eng. Sci. **58**, 1463 (2003).
[35] M. V. Wickerhauser, *Adapted Wavelet Analysis from Theory to Software* (A. K. Peters, Wellesley, MA, 1994).
[36] A. K. M. F. Hussain, Phys. Fluids **26**, 2816 (1983).
[37] J. E. Ruppert-Felsot, MS thesis, The University of Texas at Austin, 2003.
[38] M. Raffel, C. Willert, and J. Kompenhans, *Particle Image Velocimetry: A Practical Guide* (Springer-Verlag, Berlin, 1998).
[39] E. E. Michaelides, J. Fluids Eng. **119**, 233 (1997).
[40] A. M. Fincham and G. R. Spedding, Exp. Fluids **23**, 449 (1997).
[41] A. Fincham and G. Delerce, Exp. Fluids **29**, S13 (2000).
[42] K. Okamoto, S. Nishio, T. Saga, and T. Kobayashi, Meas. Sci. Technol. **11**, 685 (2000). This work describes image generation for PIV and CIV algorithm evaluation;http://piv.vsj.or.jp/piv/
[43] A. K. Prasad, Exp. Fluids **29**, 103 (2000).
[44] J. Pedlosky, *Geophysical Fluid Dynamics*, 2nd ed. (Springer-Verlag, New York, 1987).
[45] W. H. Press, B. P. Flannery, S. A. Teukolsky, and W. T. Vetterling, *Numerical Recipes in C: The Art of Scientific Computing* (Cambridge University Press, New York, 1988).
[46] L. N. Trefethen, *Spectral Methods in Matlab* (SIAM, Philadelphia, 2000).
[47] See EPAPS Document No. E-PLEEE8-71-103504 for the auxiliary materials. A direct link to this document may be found in the online article's HTML reference section. The document may also be reached via the EPAPS homepage (http://www.aip.org/pubservs/epaps.html) or from ftp.aip.org in the directory /epaps/. See the EPAPS homepage for more information.
[48] T. Acharya and P.-S. Tsai, *JPEG 2000 Standard for Image Compression* (Wiley-Interscience, Hoboken, NJ, 2005).
[49] http://jpeg.org/jpeg2000/index.html